A teamwork promotion of formin-mediated actin nucleation by Bud6 and Aip5 in *Saccharomyces cerevisiae*

Ying Xie†, Feng Zhou†, Qianqian Ma†, Lanyuan Lu*, and Yansong Miao*
School of Biological Sciences, Nanyang Technological University, Singapore 637551, Singapore

ABSTRACT **Actin nucleation is achieved by collaborative teamwork of actin nucleator factors (NFs) and nucleation-promoting factors (NPFs) into functional protein complexes. Selective inter- and intramolecular interactions between the nucleation complex constituents enable diverse modes of complex assembly in initiating actin polymerization on demand. Budding yeast has two formins, Bni1 and Bnr1, which are teamed up with different NPFs. However, the selective pairing between formin NFs and NPFs into the nucleation core for actin polymerization is not completely understood. By examining the functions and interactions of NPFs and NFs via biochemistry, genetics, and mathematical modeling approaches, we found that two NPFs, Aip5 and Bud6, showed joint teamwork effort with Bni1 and Bnr1, respectively, by interacting with the C-terminal intrinsically disordered region (IDR) of formin, in which two NPFs work together to promote formin-mediated actin nucleation. Although the C-terminal IDRs of Bni1 and Bnr1 are distinct in length, each formin IDR orchestrates the recruitment of Bud6 and Aip5 cooperatively by different positioning strategies to form a functional complex. Our study demonstrated the dynamic assembly of the actin nucleation complex by recruiting multiple partners in budding yeast, which may be a general feature for effective actin nucleation by formins.**

Monitoring Editor
Thomas Pollard
Yale University

Received: Jun 2, 2021
Revised: Nov 8, 2021
Accepted: Nov 16, 2021

INTRODUCTION

Dynamic actin assembly requires collaborative recruitment of multiple actin monomers by paired actin nucleation factors (NFs) and nucleation promoting factors (NPFs) that spatiotemporally regulate actin polymerization for a multitude of cellular activities (Pollard, 2007; Quinlan *et al.*, 2007; Chesarone and Goode, 2009; Firat-Karalar and Welch, 2011; Zoncu *et al.*, 2011; Breitsprecher *et al.*, 2012; Graziano *et al.*, 2013; Xie *et al.*, 2019). Several NPFs have been known to promote NF-mediated actin nucleation via tunable protein interactions and composition stoichiometry of the formed nucleation complex, such as Wiskott–Aldrich syndrome protein (WASP) and WAVE (WASP family veroprolin homolog) regulatory complex (WRC) for Arp2/3 complex in diverse eukaryotes, as well as Bud6 and Aip5 for yeast and fungal formins (Quinlan *et al.*, 2007; Graziano *et al.*, 2011; Tu *et al.*, 2012; Xie *et al.*, 2020; Zheng *et al.*, 2020). In addition, the hierarchical assembly of multiple participating partners was shown to result in macromolecular condensation of WASP that exhibited enhanced NPF activity (Campellone *et al.*, 2008; Padrick *et al.*, 2008; Sallee *et al.*, 2008; Su *et al.*, 2016; Case *et al.*, 2019). Such synergistic nucleation of F-actin was also demonstrated by the association of two NFs or the interactions of two NPFs on the same NF, such as Spire-Fmn2/Capu, adenomatous polyposis coli (APC)-mDia1, and Aip5-Bud6-Bni1 (Machesky *et al.*, 1999; Moseley and Goode, 2005; Quinlan *et al.*, 2007; Okada *et al.*, 2010; Graziano *et al.*, 2011; Bieling *et al.*, 2019; Case *et al.*, 2019; Glomb *et al.*, 2019; Xie *et al.*, 2019). In *Drosophila melanogaster*, the WASP homology 2 class-NF Spire synergizes with the actin nucleation activity

This article was published online ahead of print in MBoC in Press (http://www.molbiolcell.org/cgi/doi/10.1091/mbc.E21-06-0285) on November 24, 2021.

†These authors contributed equally.

Conflict of interest: The authors declare that they have no conflicts of interest in regard to this article.

*Address correspondence to: Lanyuan Lu (LYLU@ntu.edu.sg); Yansong Miao (yansongm@ntu.edu.sg).

Abbreviations used: APC, adenomatous polyposis coli; CD, circular dichroism; IDR, intrinsically disordered region; LatA, latrunculin A; MD, molecular dynamics; NF, nucleation factor; NPF, nucleation promoting factor; PCA, principal component analysis; RMSD, root-mean-square deviation; WASP, WASP family veroprolin homolog; WAVE, Wiskott–Aldrich syndrome protein; WRC, WAVE regulatory complex.

of formin class-NF Cappuccino (Quinlan *et al.*, 2007; Vizcarra *et al.*, 2011). In mammalian cells, APC protein has applied the rocket launcher mechanism to boost the nucleation activity of formin mDia1 (Okada *et al.*, 2010; Breitsprecher *et al.*, 2012). Recently, Aip5 was identified as another fungal NPF for Bni1 in both *Saccharomyces cerevisiae* and *Candida albicans* by binding to actin monomer and Bni1 through its C-terminus (1110–1234 a.a for ScAip5C and 786–896 a.a for CaAip5C) (Xie *et al.*, 2019, 2020); *aip5*Δ exhibited synthetic sickness in the background of *bni1*Δ, suggesting a potential function of Aip5 in collaborating with the remaining formin Bnr1 in *bni1*Δ. Interestingly, while the C-terminal tail of Bni1 (1767–1953 a.a) hosts both NPFs, Aip5 and Bud6, for complex formation, Bnr1 likely works with NPFs differently because the C-terminal intrinsically disordered region (IDR) of Bnr1 is much shorter (1288–1375 a.a) than Bni1-C (1767–1953 a.a) and does not seem to interact with Bud6 on its own (Graziano *et al.*, 2013). The active region of NPF Bud6, Bud6C (residues 489–788), is located close to the FH2 domain of Bnr1, which thereby impairs NPF function if not recruiting the alleviation factor Bil1 (Graziano *et al.*, 2013). Due to the intrinsically disordered nature of both formin's C-terminal tails, it has also been challenging to determine the structural position of Bud6C and Aip5C in the Bni1-Bud6-Aip5 complex in coordinating their interactions and activities. Thus, how actin cables were nucleated by collaborative pairing for two distinct nucleators, Bni1 and Bnr1, and two NPFs, Aip5 and Bud6, into NPF-NF complexes has remained enigmatic.

Here we unraveled a common paradigm of orchestrated actin cable nucleation from the partnership of a formin, Bni1 or Bnr1, with two NPFs, Bud6 and Aip5, in budding yeast. *In vitro* biochemical assays and in vivo genetics have validated the collaborative functions of two NPFs, Aip5 and Bud6, on distinct formins. Through molecular dynamics (MD) simulation, we obtained interactive modes for two sets of NF-NPF complexes in which each component could adopt an appropriate conformation to avoid steric hindrance for efficient nucleation of actin cables. We also found that unlike Bni1-C, a helix of the Bnr1 FH2 region is required to stabilize its tri-protein complex. Our results shed light on the orchestrated complex formation of yeast formin NFs and NPFs, which might be a general mechanism underlying actin assembly in the fungal kingdom.

RESULTS

Aip5 is a nucleation-promoting factor for both Bni1 and Bnr1

To investigate whether Aip5 has conversed NPF activities for both yeast formins, Bni1 and Bnr1, we examined actin nucleation biochemically using the recombinant protein domain of Aip5 (Aip5C, residues 1110–1234 a.a.), Bni1 (Bni1FH1C, residues 1227–1953 a.a.), and Bnr1 (Bnr1FH1C, residues 757–1375 a.a.), in the presence of Pfy1 (Supplemental Figure S1, A–C). Consistent with previously reported results, Bnr1FH1C stimulated actin polymerization in a bulk actin assembly assay in a dose-dependent manner in the presence of profilin (Figure 1, A and B and Supplemental Figure S1D) (Moseley and Goode, 2005). Interestingly, we observed that Aip5C is capable of promoting the actin nucleation of both Bni1FH1C and Bnr1FH1C in an Aip5 dose-dependent manner (Figure 1, A and B). By analyzing the half polymerization of actin polymerization, Aip5C exhibited a slightly higher potency in stimulating Bni1 than Bnr1 for actin nucleation (Figure 1, C and D).

Because Aip5C directly interacts with Bni1-C (residues 1767–1953 a.a.) (Xie *et al.*, 2019), we next examined whether Aip5C similarly interacts with Bnr1. Using a fluorescence anisotropy binding assay, we found that Bnr1-C directly interacts with Aip5C at a K_D of 237 ± 43 nM (Figure 1E), although Bnr1-C (residues 1288–1375 a.a.) is much shorter than the corresponding IDR of Bni1-C (Supplemental Figure S1, A, B, and E). In addition, Bnr1FH1C displayed a stronger affinity and positive cooperativity to Aip5 than Bnr1-C with a K_D of 82±12 nM (Figure 1E), reminiscent of the similar interactions between Aip5C and Bni1FH1C (Xie *et al.*, 2019). To further confirm the different promotion effects of Aip5C on the two formins, we next utilized a total internal reflection fluorescence (TIRF) actin polymerization assay to determine the Aip5C functions in formin-mediated nucleation in the presence of profilin (Pfy1). First, 10 nM Bni1FH1C and 2 nM Bnr1FH1C displayed similar nucleation activity, both of which generated ~5-fold more actin seeds than the control of profilin-actin at the initial period of polymerization (Figure 1, F and G). In the presence of 20 nM Aip5C, Bni1FH1C- and Bnr1FH1C-initiated actin nucleation was significantly enhanced by ~1.73- and ~1.69-fold, respectively (Figure 1, F and G). This observation agreed with the bulk actin assembly result, where Aip5C promoted both Bni1- and Bnr1-mediated actin polymerization (Figure 1, A–D). By examining the actin filament elongation rate over 5 min, Aip5C did not alter the barbed end elongation for Bni1FH1C- or Bnr1FH1C in the presence of Pfy1 (Figure 1, F and H), indicating an NPF function of Aip5C for both yeast Bni1 and Bnr1.

Teamwork efforts of Aip5 and Bud6 on formin nucleation activity

Bud6 is a well-studied NPF for budding yeast Bni1 and Bnr1 (Moseley and Goode, 2005; Graziano *et al.*, 2011; Tu *et al.*, 2012; Graziano *et al.*, 2013). We next sought to investigate whether Aip5 cooperates with Bud6 to boost formin-mediated actin nucleation. We first used a pyrene actin assembly assay to examine actin polymerization under different combinations of NFs and NPFs using the short C-terminus of Bud6 (Bud6C, residues 550–789 a.a.), which is sufficient to activate Bnr1 without hindering the FH2 domain and masking its activity in actin nucleation (Graziano *et al.*, 2013). In the presence of Pfy1, Bud6C enhanced actin polymerization triggered by Bni1 and Bnr1 in the pyrene actin assay (Figure 2, A and B). Interestingly, an additional supplement of Aip5C to the protein mixtures of formins and Bud6C further activated actin polymerization (Figure 2, A and B). To distinguish the roles of Aip5 and Bud6 in formin-mediated nucleation and elongation, we performed a TIRF actin polymerization assay. We found that Aip5C promoted the nucleation activity of both Bni1-Bud6 without altering the barbed end elongation in the presence of Pfy1 (Figure 2, C–E and Supplemental Movie S1). Compared with Bni1FH1C-mediated actin nucleation in the presence of Bud6C, additional Aip5C resulted in an ~3.4-fold increase in the generation of actin seeds, whereas Aip5C enhanced Bnr1FH1C-Bud6C-mediated actin nucleation by ~1.13-fold (Figure 2, C and D). The presence of two NPFs showed higher promotion rates on Bni1 (~3.9-fold)- and Bnr1 (~2.1-fold)-mediated nucleation than one NPF, Bud6C, or Aip5C. The NPF-NF pairs showed a 1.3-2-fold increase in their promotion of NF activity (Figures 1, F and G and 2, C and D). The above results indicate the teamwork of two NPFs on Bni1 by working simultaneously. However, Bni1 and Bnr1 showed slightly different modes of partnership with the two NFPs. Aip5C and Bud6C showed a synergistic effect on Bni1FH1C by having a combined promotion rate (~3.9-fold) that was greater than the multiplied rates from two single NFPs, Aip5C (~1.73-fold) and Bud6C (~1.23-fold), on their own. (Figure 1, F and G, and Figure 2, C and D). However, the overall promotion rate of the two NFPs on Bnr1FH1C (~2.1-fold) was slightly lower than the multiplied rates (~ 3.5) of Bud6C (~1.83) and Aip5C (~1.69), indicating an additive effect instead of a synergy of the two NPFs on Bnr1 (Figure 1, F and G and Figure 2, C and D).

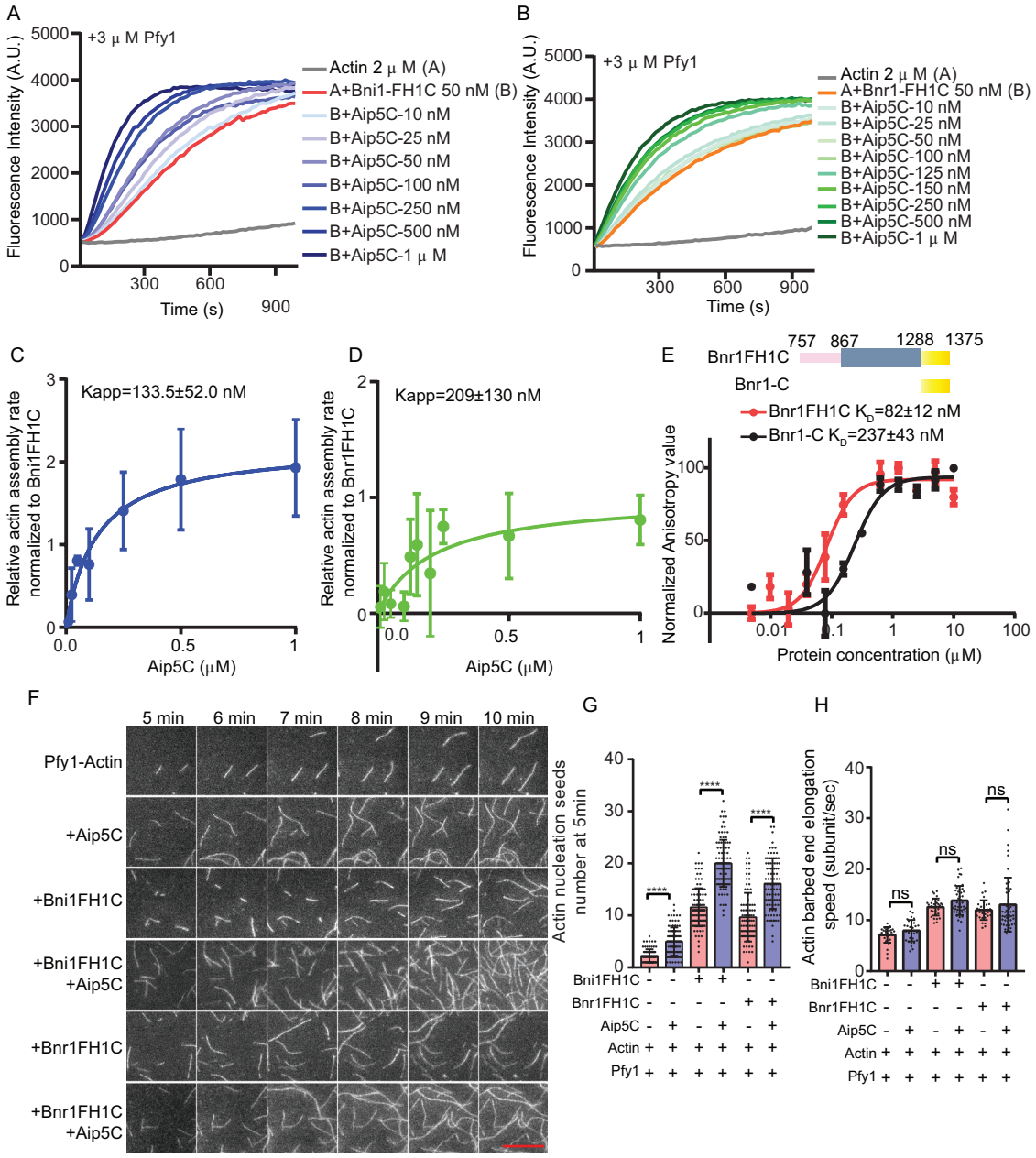

FIGURE 1: Aip5 binds to both Bni1 and Bnr1 and stimulates their nucleation activities. (A, B) Pyrene actin polymerization of 2 μM G-actin with 3 μM yeast Pfy1. An increasing amount of Aip5C was added to 50 nM of Bni1FH1C and Bnr1FH1C, respectively, at the indicated concentrations. (C, D) The relative actin assembly rates of Aip5C were normalized to Bni1FH1C and Bnr1FH1C, respectively, where the K_{app} was deduced from three independent biological replicates. (E) Fluorescence anisotropy binding measurements of Aip5C (Alexa 488 labeled, 30 nM) that were titrated by a serial concentration of Bnr1FH1C and Bnr1-C, respectively, as indicated. Data are represented by circles using the average value of three biological replicates and fitted by the Hill equation to determine the K_D. (A.U., arbitrary unit.). (F) The representative TIRF images of actin nucleation seeds formed at 5 and 10 min, respectively. The control actin filament was assembled from 1 μM actin (10% Oregon green 488-labeled actin and 0.5% biotin-actin) with 3 μM yeast Pfy1, and the used proteins were indicated as follows: 10 nM Bni1FH1C; 2 nM Bnr1FH1C and 20 nM Aip5C. The scale bar represents 10 μm. (G) Quantification of actin nucleation by measuring the seeds number at 5 min with the indicated combinations of proteins. (n = 86, 98, 114, 100, 94, 99 for each sample from ROI = 894 μm^2) (H) Quantification of actin filament barbed end elongation speed of indicated protein combinations as shown in A. (n = 31, 30, 31, 45, 31, 49 for each sample) P values was determined by the one-way ANOVA, ns = not significant, $^{**}p < 0.01$, $^{****}p < 0.0001$. Error bar, SD.

To further understand the teamwork modes of the two NPFs on one NF, we performed an anisotropic assay to characterize the change in interactions between Aip5 and formin by supplementation with Bud6.

We previously characterized NFs and NPFs in vivo to understand their physiologically relevant range of concentrations and stoichiometry at their concentrated sites. In vivo Aip5 and Bni1 have a concentration of 120 nM and 80 nM, respectively, at the

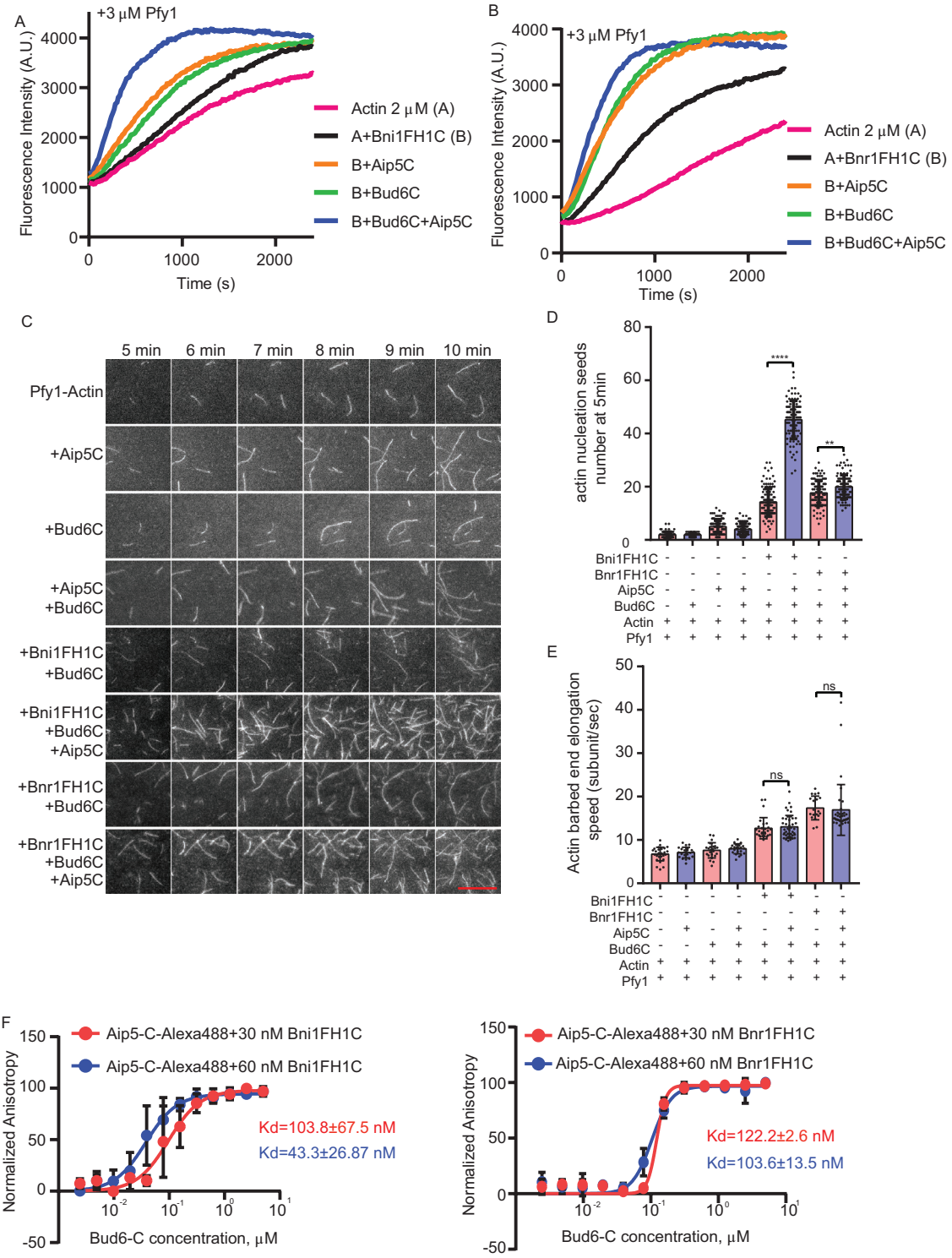

FIGURE 2: Aip5 and Bud6 synergizes formin-mediated actin nucleation. (A, B) Pyrene actin polymerization with different combinations of proteins as indicated, 2 μM monomeric actin, 3 μM yeast profilin, 200 nM Aip5C, 40 nM Bud6C, 20 nM Bni1FH1C, and 20 nM Bnr1FH1C. (C) The representative TIRF images of actin nucleation seeds formed from 5 to 10 min using the indicated combination of proteins. The actin filament was assembled by mixing 1 μM actin (10% Oregon green 488-labeled actin and 0.5% biotin-actin) with 3 μM yeast profilin, 10 nM Bni1FH1C, 2 nM Bnr1FH1C, 5 nM Bud6C, or 20 nM Aip5C. The scale bar represents 10 μm. (D) Quantification of actin nucleation seeds number at 5 min with the indicated combinations of proteins (n = 80, 60, 98, 94, 114, 99, 100, 100 for each sample from ROI = 894 μm^2). (E) Quantification of actin filament barbed end elongation speed of indicated protein combinations as shown in A (n = 28, 21, 24, 23, 27, 43, 19, 37 for each sample). (F) Fluorescence anisotropy binding measurements of 60 nM Alexa 488-labeled Aip5C were preincubated with different concentrations of Bni1FH1C and Bni1FH1C, respectively, before being titrated by a serial concentration of Bud6C. P values was determined by the one-way ANOVA, ns = not significant, ****$p < 0.0001$. Error bar, SD.

bud tip (Xie *et al.*, 2019). To inform the design of biochemical assays comparing the nucleation activities of two formin-NPF complexes, Bni1-Aip5-Bud6 and Bnr1-Aip-Bud6, and facilitate the interpretation of their physiological relevance, we determined a Bud6 concentration of ~100 nM at the bud tip and a Bnr1 concentration of ~200 nM at the bud neck (Supplemental Figure S1F), as previously reported for the determination of in vivo Bni1 and Aip5 (Xie *et al.*, 2019). Bni1 and Bnr1 have differential localizations during early polar growth. Aip5 and Bud6 could switch their localization from the bud tip to the neck along with cell cycle progression. We measured the concentrations of the two formins at both the tip and the neck. In contrast, we only measured Aip5 and Bud6 concentrations at one location to simplify the stoichiometry estimation of NF-NPFs at a snapshot moment along the cell cycle without considering the migration of Aip5 and Bud6. The C-terminal fragment of Aip5 (1000–1234) has been shown to interact with the N-terminal fragment of Bud6 (1–141) (Glomb *et al.*, 2019), indicating the intermolecular interaction between Bni1, Aip5, and Bud6 as a tri-protein nucleation complex. It is technically challenging to express and purify all these full-length formin and NPF proteins using our current prokaryotic expression system. It is challenging to examine complex formations with full lengths with all possible interactions. Hence we used a minimum-component reconstitution approach to dissect the molecular mechanism by which two NPFs work on one formin simultaneously. We reconstituted the tri-protein complex interaction using fragments of Aip5C and Bud6C, which contain the formin-binding NPF domains of each protein but lack the domains known to mediate interactions between Aip5 and Bud6 (Glomb *et al.*, 2019). It is possible that these domains could even further elevate the collaborative NPF effects of Aip5 and Bud6 on formins. Here we added increasing concentrations of Bud6C to the premixed sample of Alexa 488-labeled Aip5C and Bni1FH1C in which the changes in anisotropic value would likely reflect the interaction changes between Aip5 and Bni1FH1C-Bud6C. Notably, all three proteins used here are in their dimeric state (Moseley *et al.*, 2004; Xu *et al.*, 2004; Tu *et al.*, 2012; Garabedian *et al.*, 2018; Xie *et al.*, 2019). We found that Bud6C started to obviously enhance the anisotropy signal of Aip5 (60 nM) and Bni1 (30 nM) from a lower concentration and stoichiometry than for the pair of Aip5 (60 nM) and Bnr1 (30 nM). A likely explanation is that the interactions between Aip5 and Bni1FH1C are stimulated by the presence of Bud6C, starting from the concentrations of ~30 nM Bud6C, which has a Bni1FH1C:Aip5C:Bud6C stoichiometry of 1:2:1 (Figure 2F). However, we could not exclude the possibility that the tumbling rate of Aip5C was changed simply by the increasing partition of Bud6C within the macromolecular complex. Interestingly, a higher Bni1FH1C:Aip5C stoichiometry at 1:1 (60 nM each) demonstrated a further enhanced interaction in response to increasing concentrations of Bud6C, such as 60 nM Bud6C:Bni1FH1C:Aip5C at a stoichiometry of 1:1:1. The above results suggest that Bni1C has sufficient binding sites to host both Aip5C and Bud6C, creating a joint effort of two NPFs toward a formin protein. In contrast, Bud6C exhibited slower promotion effects on the mix of Aip5C and Bnr1FH1C, which only started to show noticeable enhancement in interactions after adding more than 200 nM of Bud6C even under conditions with twice the amount of Bnr1 at 60 nM (Figure 2F). The different binding kinetics of Bni1-Aip5 and Bnr1-Aip5 in response to Bud6 also indicated distinct interaction modes within the two tri-protein nucleation complexes, similar to their different activities in nucleating actin polymerization (Figure 2, C and D).

MD simulation of the complex conformation of formin-Bud6-Aip5

Since Aip5 and Bud6 collaboratively activate both formins, we next sought to understand the conformation and the orchestral functions of two different sets of tri-protein complexes. Because it is challenging to obtain structural information on the tri-protein complex by protein structural studies, due to the flexible nature of formin C-terminal IDR, we used an all-atom MD simulation. We utilized Bni1-C and the functional and structural regions of the NPFs Aip5C (PDB: 6ABR) (Xie *et al.*, 2019) and Bud6^{core} (residues 550–688 a.a., PDB: 3ONX) (Tu *et al.*, 2012) (Figure 3A) for MD simulation. We assigned the initial structure of Bni1-C as a random coil (Figure 3A) due to its IDR nature (Xie *et al.*, 2019). We placed Bud6^{core} and Aip5C at eight different initial positions relative to Bni1-C in MD simulations to avoid bias by using specific relative positioning. All MD simulations converged after 200 ns, as shown by root-mean-square deviation (RMSD) plots (Supplemental Figure S2A), suggesting a relatively stable complex conformation. The representative conformations of the tri-protein complex were determined by choosing the lowest free energy conformation from the two-dimensional free energy surface made by principal component analysis (PCA) (Supplemental Figure S2B). To further compare the relative stabilities of the eight low free energy conformations, we calculated the scores of the conformations by the Rosetta program (Alford *et al.*, 2017) (Supplemental Figure S2C) where the most stable Bni1-Bud6-Aip5 tri-protein complex with the lowest Rosetta scores is shown in Figure 3B. Interestingly, Aip5C preferentially associates with the C-terminus part of Bni1-C, whereas Bud6^{core} interacts more toward the N-terminus of the C-terminal tails of Bni1-C (Figure 3C). We did not observe close contact between Bud6^{core} and Aip5C, which is consistent with the result tested by fluorescence polarization (Supplemental Figure S2D). Furthermore, Aip5 C-terminus (residues 1000–1234 a.a.) was reported to associate with the N-terminus of Bud6 (residues 1–141 a.a.) (Glomb *et al.*, 2019).

A similar strategy of MD simulation was applied to study the Bnr1-Bud6-Aip5 tri-protein complex conformation. Although the C-terminal regions of both formins are essential for direct binding with Aip5C, Bnr1-C (1288–1375 a.a.) alone is insufficient to interact with Bud6C (Figure 4A) (Graziano *et al.*, 2013). This is consistent with the previously identified Bnr1 FH2 domain as the interactive domain in association with Bud6C. Nevertheless, the NPF activity of Bud6 still requires the C-terminus tail of Bnr1 (Graziano *et al.*, 2013). By observing the resolved crystal structure of the Bni1 FH2 domain (PDB: 1UX5), there is a long αT helix extending out from the "doughnut"-shaped structure, and such an αT helix is conserved in Bnr1 (residues 1247–1288 a.a.) (Supplemental Figure S3, A and B) (Xu *et al.*, 2004). Hence we hypothesized that the αT helix of Bnr1 that is adjacent to the C-terminus might be crucial to interact with Bud6C directly. Thus we constructed another Bnr1 C-terminus variant, which includes the αT helix (Bnr1-LC, residues 1247–1375 a.a.). Indeed, we found that Bnr1-LC displayed a high affinity and positive cooperativity in interacting with Bud6C (Figure 4A). A circular dichroism (CD) analysis also showed an ~40% increase in the alpha-helix conformation of Bnr1-LC compared with Bnr1-C (Supplemental Figure S3, C and D). Based on the above experimental results, we ran MD simulations for Bnr1-LC by assigning an α-helix followed by a random coil as the initial structure (Figure 4B). Similar to the MD simulation setup for the Bni1-Bud6-Aip5 tri-protein set, we placed Bud6^{core} and Aip5C at eight different initial positions relative to Bnr1-LC. The representative stable complexes, which were evaluated by RMSD, were chosen from all simulation trajectories using free energy analysis by PCA (Supplemental Figure S4, A and B). Furthermore, Rosetta

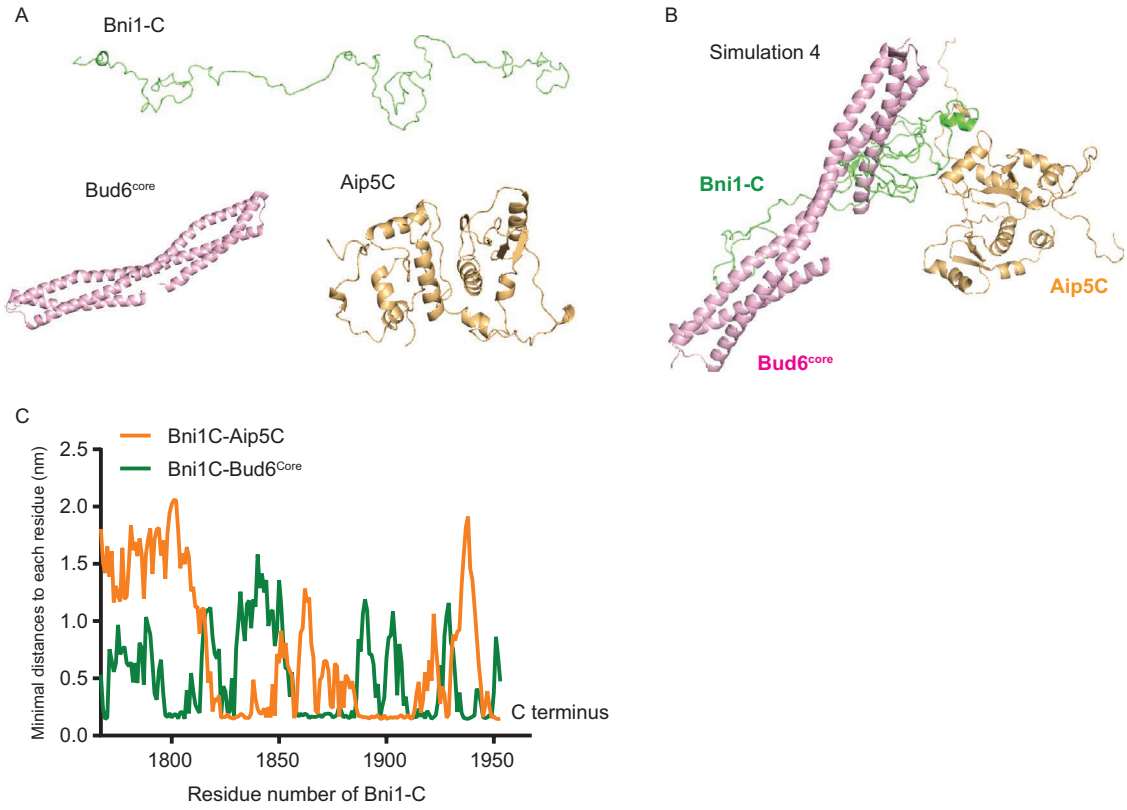

FIGURE 3: Computer simulation of the complex assembly of Bni1-Bud6-Aip5. (A) Initial structures of Bni1-C, Aip5C, and Bud6^{core} for setting up the MD simulations. (B) The most stable complex conformation (Simulation 4 in Supplemental Figure S2) from MD simulations among the eight randomly positioned nucleation complexes (Bni1-C, green; Aip5C orange; Bud6C, pink). (C) The minimal distance plot of each residue of Bni1-C from Aip5C (orange) and Bud6^{core}(green), respectively, in the complex conformation in B.

scoring identified the most stable Bnr1-Bud6-Aip5 tri-protein complex from the eight simulated conformations (Figure 4C and Supplemental Figure S4C). Interestingly, the Aip5C protein preferentially associates with the C-terminus part of Bnr1-LC, similar to what we observed in the Bni1-Bud6-Aip5 tri-protein complex, whereas Bud6^{core} associates more toward the N-terminus region adjacent to the αT helix in the Bnr1-LC (Figure 4D), suggesting a potential role of the αT helix in stabilizing the interaction between Bud6^{core} and Bnr1-C, consistent with the experimentally validated interaction between Bnr1-LC and Bud6C (Figure 4A). To further test this hypothesis, we performed MD simulations of the interactions between the αT helix-lacking Bnr1-C, Bud6^{core}, and Aip5C starting from the initial positioning the same as the most stable Bnr1-LC complex in Figure 4, B and C (Figure 4E and Supplemental Figure S4, D and E). In the results, the simulation showed that by lacking the αT helix, Bnr1-C is located further away from the Bud6^{core} with reduced direct contacts compared with Bnr1-LC (Figure 4, F–H). In general, for each simulated NF-NPF pair, electrostatic interactions and hydrogen bonds contribute to the majority of interactions (Supplemental Figure S5).

Aip5 regulates actin cable formation in vivo with formins and Bud6

To investigate the in vivo teamwork effort of Bud6 and Aip5 in promoting formin-mediated actin nucleation, we generated multiple single/double/triple mutants that knocked out different NFs and NPFs. Notably, the triple mutant *bni1*Δ *aip5*Δ *bud6*Δ, which deleted three polarisome components, was lethal, suggesting an essential function of three NF-NPF proteins for cell physiology (Supplemental Figure S6A). Subsequently, we tested the cell growth of different mutants in the presence of a low dose of 1 μM latrunculin A (LatA), which slightly disrupts the actin cytoskeleton (Supplemental Figure S6, B–D) (Miao *et al.*, 2013, 2016). To compare the sensitivity of different mutants to actin perturbation, we measured the area size under each growth curve, which was used to calculate the ratio change between growth conditions with or without LatA (Figure 5A and Supplemental Figure S6, E and F). Under such a mild perturbation in actin polymerization, wild-type yeast reduces cell growth by ~10%. However, *aip5*Δ exhibited high sensitivity to LatA treatment in which we observed an ~40% growth reduction, which was the highest growth retardation among all the single mutants (Figure 5A); *bni1*Δ and *bnr1*Δ led to only an approximately 20–30% reduction in growth on F-actin perturbation (Figure 5A). Further removal of *AIP5* in any NF or NPF mutant attributed to an additional sensitivity to LatA by a further decrease in growth rate (Figure 5A), supporting the crucial function of Aip5 in F-actin turnover by itself and cooperation with other nucleation regulatory factors. The above observations are consistent with the dual roles of Aip5 in budding yeast as an NPF for formins and a weak NF (Xie *et al.*, 2019). When comparing different double mutants, the removal of *BUD6* or *AIP5* seems to provide different sensitivity to LatA treatment in the background that deletes different formins. The triple mutants *bnr1*Δ *aip5*Δ *bud6*Δ demonstrated the greatest extent of genetic sickness in the presence of LatA. Because the triple mutant lacks functional assembly of both formin complexes, Bni1-NPFs and Bnr1-NPFs, our results suggest the teamwork function of the two NPFs in regulating Bnr1-mediated actin turnover for cell growth. To better characterize the protein

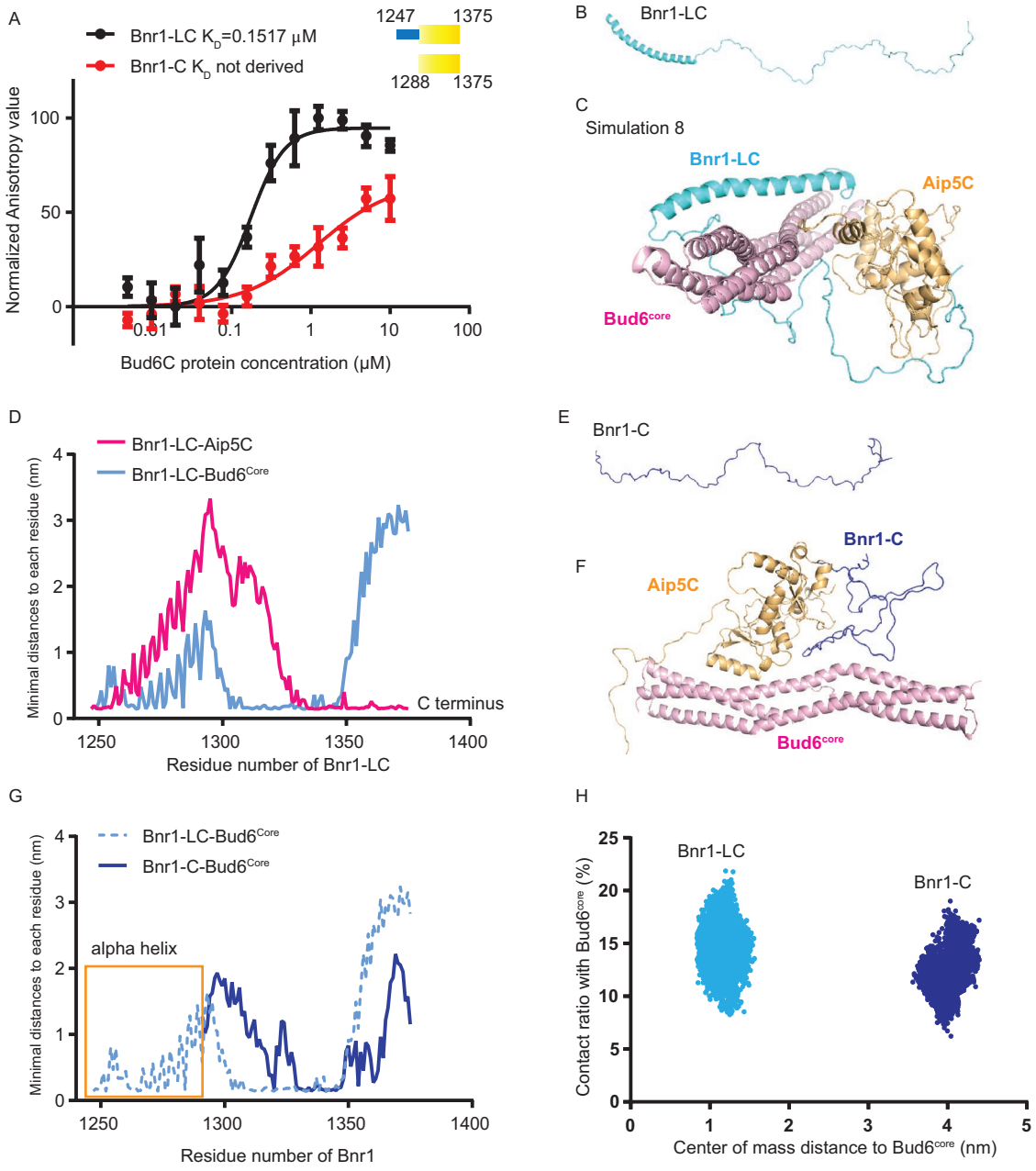

FIGURE 4: Computer simulation of the complex assembly of Bnr1-Bud6-Aip5. (A) Fluorescence anisotropy binding measurements of Alexa 488-labeled Bnr1-LC (1245-1375 a.a., 30 nM) and Bnr1-C (1288-1375 a.a., 30 nM) by a serial concentration of Bud6C, respectively. The average values from three biological replicates are fitted by the Hill equation to determine the K_D. (A.U., arbitrary unit.). (B) The initial structure of Bnr1-LC. (C) The most stable complex conformation (Simulation 8 in Supplemental Figure S4) among the eight sets of Bnr1-Bud6-Aip5 MD simulations (Bnr1-LC, cyan; Aip5C, orange; Bud6^{core}, pink). (D) The minimal distance plot of each residue between Bnr1-LC and Aip5C(pink)/Bud6^{core} (blue) in the final stable complex conformation, as shown in Figure 3C. (E) The initial structure of Bnr1-C. (F) The final Bnr1-C- Bud6^{core} -Aip5C complex conformation after MD simulation (Bnr1-C, blue; Aip5C, orange; Bud6^{core}, pink). (G) The minimal distance plot of each residue between Bnr1-LC (light blue, dashed curve) and Bnr1-C (dark blue, solid curve) with Bud6^{core} in the final stable complex conformation. (H) The conformational distribution of Bnr1-LC/Bnr1-C as a function of the contact ratio (percentage of residues contacting with Bud6^{core}) and the center of mass distance to Bud6^{core}.

functions in regulating actin assembly, we examined different mutants expressing the actin cable marker Abp140-3GFP. Compared with the wild type, *aip5*Δ exhibited a reduction in the population of healthy and intact actin cables by ~60%, whereas single mutants of formin lost ~70% (Figure 5, B–D). Consistent with previous findings (Graziano *et al.*, 2011), *bud6*Δ displays severe disruption of actin cables (Figure 5, B–D). Removal of *AIP5* in the mutant background of *BNR1* or *BNI1* resulted in more cells carrying depolarized actin cables by 30–50% and reduced actin cable numbers, suggesting Aip5 roles in coordinating the function of both formins in vivo (Figure 5, B–D). Together with the lethality of the *bni1*Δ *aip5*Δ *bud6*Δ triple mutant and the severe impairment of actin cable in the *bnr1*Δ

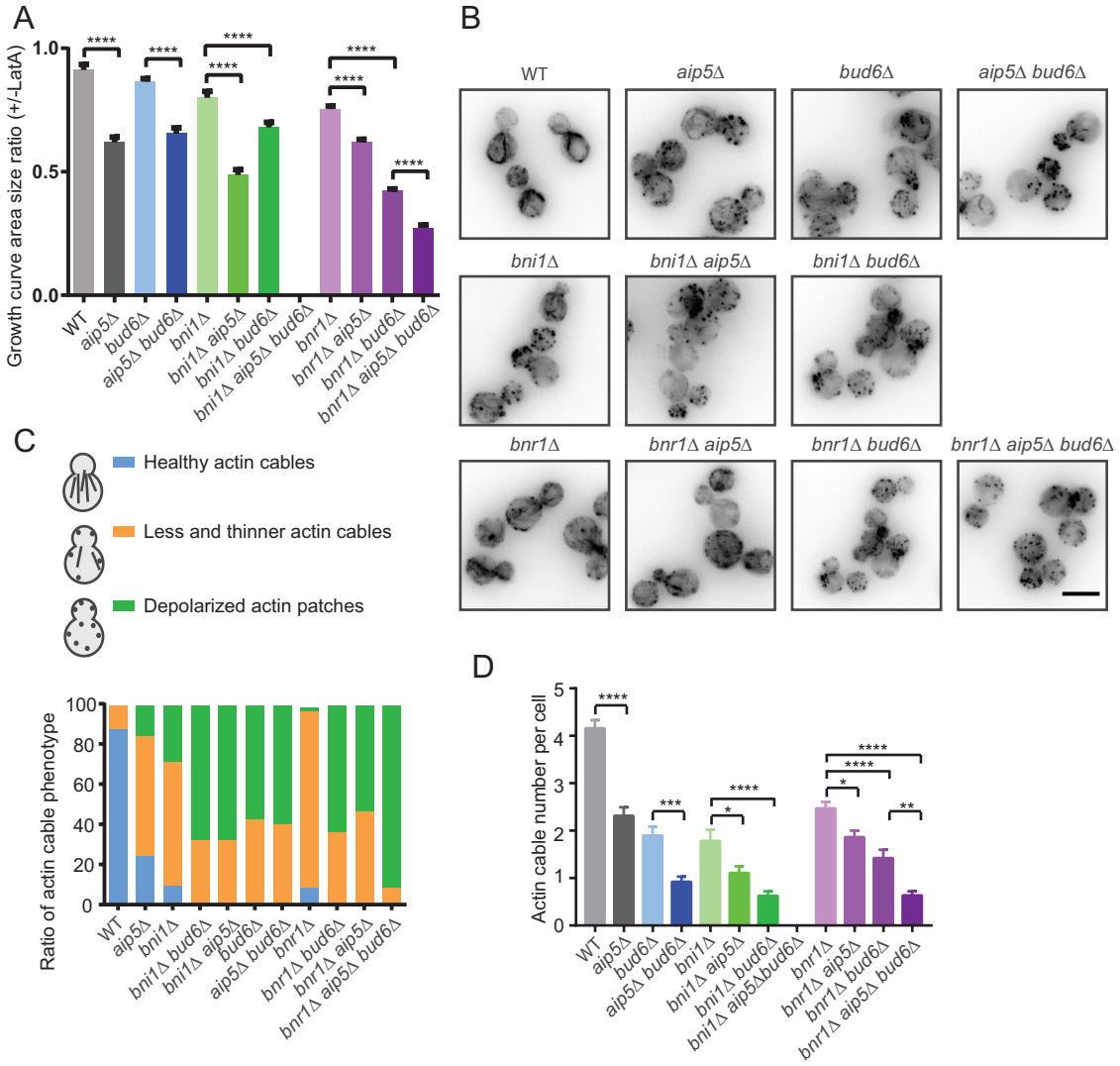

FIGURE 5: Aip5 regulates actin assembly together with formins in vivo. (A) Quantification of the area ratio of the growth curve of indicated yeast cells. The ratio is calculated by normalizing the untreated cells by 1 μM LatA-treated cells. (B) Representative fluorescence images of actin cable marker Abp140-3GFP from indicated yeast strains. The scale bar is 5 μm. (C) The overall actin cable phenotypes are characterized by normal actin cables, less and thinner actin cables, and depolarized actin cables. The cell number quantified for each strain: wild type (WT), $n = 55$; *aip5*Δ, $n = 58$; *bni1*Δ, $n = 32$; *bni1*Δ *bud6*Δ, $n = 40$; *bni1*Δ *aip5*Δ, $n = 49$; *bud6*Δ, $n = 33$; *aip5*Δ *bud6*Δ, $n = 47$; *bnr1*Δ, $n = 35$; *bnr1*Δ *bud6*Δ, $n = 49$; *bnr1*Δ *aip5*Δ, $n = 52$; *bnr1*Δ *bud6*Δ *aip5*Δ, $n = 45$. (D) Actin cable number analysis in different yeast strains in (B). Error bar, SE; From left to right: wild type (WT), $n = 63$; *aip5*Δ, $n = 70$; *bni1*Δ, $n = 58$; *bni1*Δ *bud6*Δ, $n = 79$; *bni1*Δ *aip5*Δ, $n = 60$; *bud6*Δ, $n = 115$; *aip5*Δ *bud6*Δ, $n = 105$; *bnr1*Δ, $n = 79$; *bnr1*Δ *bud6*Δ, $n = 133$; *bnr1*Δ *aip5*Δ, $n = 65$; *bnr1*Δ *bud6*Δ *aip5*Δ, $n = 118$ cells.

*bud6*Δ *aip5*Δ mutant (Figure 5, B–D), our results suggest indispensable tricomponent complex assembly for forming the nucleation core of NF-NPFs underlying actin cable polymerization and cell growth for both Bni1 and Bnr1.

DISCUSSION

Common machinery of cooperative actin nucleation

Actin nucleation is a complex and tunable process regulated by the assembly of NFs and their binding partners. Increasing evidence has demonstrated a common mechanistic framework in which collaborative actin nucleation can be achieved by the multimerization of NPFs or by multicomponent participation. Such teamwork in actin nucleation by different combinations of NFs and NPFs requires the generation of biomolecular complexes that are assembled at lower or higher orders depending on the interaction modes of the complex components. There are many reports in which protein oligomerization creates local connectivity and cooperativity of NF or NPFs, thereby increasing nucleation activities. Dynamic interplays could occur between different NFs in which a joint effort of NFs was implemented for actin nucleation and elongation, such as Formin Cappuccino-Spir and mDia1-APC (Quinlan *et al.*, 2007; Okada *et al.*, 2010; Pfender *et al.*, 2011; Breitsprecher *et al.*, 2012). Several types of multimerization of NPF have also been shown to enhance nucleation activity, such as dimerization of WASP by GST tagging (Higgs and Pollard, 2000) and WASP clustering by the pathogen effector EspFU (Sallee *et al.*, 2008) or SNX9 (Yarar *et al.*, 2007). Furthermore, processive actin polymerase Ena/VASP family proteins were found to enhance their activities in processive actin elongation once

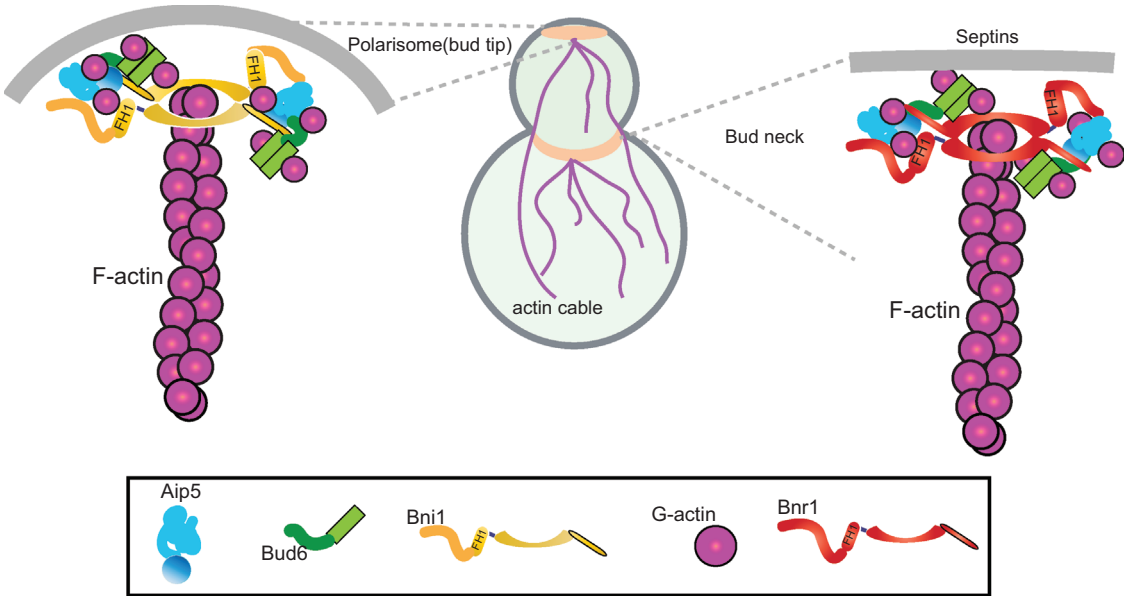

FIGURE 6: NF-NPFs complex for Bni1 and Bnr1 in budding yeast. Bud tip and bud neck localized formin Bni1 and Bnr1, respectively, form tricomponents complex with Aip5 and Bud6 dimers for barbed end nucleation in budding yeast.

clustered by IRSp53 (insulin receptor substrate of 53 kDa) (Disanza *et al.*, 2013; Brühmann *et al.*, 2017; Cheng and Mullins, 2020). Fascin-mediated F-actin bundling also increases the processivity of the nucleator Ena/VASP (Harker *et al.*, 2019), likely through a similar mechanism that increases the location concentration of contact sites and elongates local residence times of VASP proteins. Recently, activation of immune receptor signaling triggered high-order macromolecular assembly, and condensation of WASP increased WASP dwell time locally and thereby enhanced actin nucleation, undergoing liquid-liquid phase separation (Su *et al.*, 2016; Case *et al.*, 2019).

Here we describe an additional cooperative mode in two budding yeast NPFs, Bud6 and Aip5, that jointly promote actin nucleation activities of the same formin, Bni1 or Bnr1, with different modes of interplay. Budding yeast Bud6 was identified as an effective NPF for both Bni1 and Bnr1 using its formin-binding region Bud6^{core} (residues 550–688) and G–actin-binding domain Bud6^{flank} (residues 699–788) (Tu *et al.*, 2012; Graziano *et al.*, 2013). Recently, Aip5 was found to serve as an NPF of Bni1 for nucleating actin cables in budding yeast via the C-terminal Bni1-binding region (Aip5C) (Xie *et al.*, 2019). The *C. albicans* CaAip5C (residues 786–896 a.a.) and CaBud6C (residues 411–701 a.a.) exhibited cooperative association with CaBni1-C (residues 1545–1733 a.a.) in promoting Bni1-mediated actin nucleation (Xie *et al.*, 2020). Here we found a similar orchestrated pairing for the tri-protein core of the NF-NPF complex for budding yeast Bni1 and Bnr1 and propose a consensus mode between budding yeast Bni1 and filamentous fungal Bni1 as well as between differently localized Bni1 and Bnr1 in assembling the protein core for delivering G-actin into a ring-shaped FH2 structure. One of the mechanisms we have identified is the enhanced interprotein interactions between Aip5 and formin by having Bud6 (Figure 6). However, Bud6 enhanced the affinity of Aip5 to Bni1 and Bnr1 at different kinetics. The Bni1-Aip5 pair seems to be more responsive to engaging Bud6 in changing their interactions than Bnr1-Aip5, which raised an interesting hypothesis that IDR-mediated intermolecular interactions seem to create tunable interactions, packing modes, and functions by modulating the compositional stoichiometry and changing the participating sequences.

The IDRs of Aip5 and Bud6 could drive macromolecular assembly in heterogeneous states under different cellular conditions (Miao *et al.*, 2018; Xie *et al.*, 2019; Xie and Miao, 2021). Although Aip5C does not interact with Bud6C, Aip5C interacts with the N-terminal fragment of Bud6 (1–141) (Glomb *et al.*, 2019); whether full-length Aip5 and Bud6 collaborate to promote formin function needs to be further studied to achieve a more comprehensive understanding of tunable regulation of formin activities by having higher-order assembly of the complex.

Hierarchical assembly of nucleation complexes for tunable activities

Unlike the self-clustering of NPF (WASP) for Arp2/3 complex-mediated nucleation, the cooperative assembly of two formin NPFs might create more diverse assemblies of NF-NPFs for actin polymerization on various signaling events. By having a long IDR, Aip5 proteins localize to the bud tip through inter- and intramolecular interactions with Spa2, as well as cytoplasmic condensates, which contribute to stress adaptation under ATP-depleted conditions (Xie *et al.*, 2019). Such IDR participation introduces dynamic inter- and intracomponent interactions and tunable viscoelastic properties of the macromolecular assemblies. IDRs have highly variable binding affinities for diverse modes of molecular interactions and exhibit a broad range of binding modes with biomolecules depending on the length and amino acid composition, which results in nonlinearities in inter- and intramolecular interactions (Li *et al.*, 2020; Clemens *et al.*, 2021). Our formin-NPF-based interactions all showed positive cooperativity. We still do not understand how different association states of formin-NPFs correspond to actin assembly activities. It is worth future studies to have a comprehensive understanding of how cooperative NPF activities of Aip5 and Bud6 on formins are regulated by their local concentrations, structural flexibility, functional conformation, and molecular equilibrium between the dilute phase in the cytoplasm and the dense phase around the bud neck or bud tip. Nevertheless, the functional core of both sets of the formin-Aip5-Bud6 complex in budding yeast likely requires the direct tri-protein complex formation we have described here, which defines the minimum complex core for potential higher-order assemblies.

During cell signal transduction under physiological and pathological conditions, IDR creates diverse states of macromolecular assembly in spatiotemporally regulated manners, which could provide tunable activities of functional complexes, such as NF-NFPs. It has been well documented that phase separation dynamically regulates actin nucleator activities, such as the WASP and Arp2/3 complex during immune signaling (Su *et al.*, 2016; Case *et al.*, 2019) or plant formin during bacterial infection (Sun *et al.*, 2018; Qiao *et al.*, 2019; Ma and Miao, 2020; Ma *et al.*, 2021a,b; Sun *et al.*, 2021). In both of the above scenarios, spatiotemporally regulated compositional stoichiometry plays a critical role in fine-tuning actin remodeling. While Bnr1 has a relatively stable bud neck localization, Bni1 seems to have more exchange between the dense phase (tip and bud neck) and the dilute phase (cytoplasm) (Xie and Miao, 2021). Compared with Bnr1, the dynamic molecular behavior of Bni1 might offer it a more flexible spatiotemporal association with Bud6 and Aip5 than the Bnr1 set. Therefore, Bni1 is likely more sensitive than Bnr1 to environmental perturbations, such as chemical or physical cues, which influence the diffusion, condensation, and activities of Bni1 and its NPFs at emerging bud sites or bud necks (Segal *et al.*, 2000; Ozaki-Kuroda *et al.*, 2001; Buttery *et al.*, 2007; Glomb *et al.*, 2019; Xie *et al.*, 2019). *In vivo* and in vitro reconstitution systems using the full-length recombinant proteins Aip5, Bud6, and formins might address such complex regulations of actin nucleation in budding yeast. Here our results of multimember teamwork modes for both Bni1 and Bnr1 lay a foundation for future studies of complex and tunable actin remodeling during cell signaling by changing their inter- and intramolecular interactions.

METHODS

Protein expression and purification

The *Escherichia coli* expression vectors for Bni1FH1C, Bnr1FH1C, Bnr1-C, Aip5C, and Pfy1 contain N-terminal His_6-TEV, and Bud6C is fused with N-terminal GST-Prescission-His_6-TEV. All the proteins are expressed and purified from *E. coli* (*BL21(DE3) Rosetta T1R*) as previously described (Xie *et al.*, 2019). Cells were cultured in 5 ml of TB medium (24 g/l yeast extract, 20 g/l tryptone, 4 ml/l glycerol, phosphate buffer, pH 7.4) for overnight and transferred to 1 liter of TB medium for 4–5 h culture at 37°C. Afterward, 0.5 mM isopropyl-thio-b-D-galactoside was added for protein induction at 18°C for overnight culture. The cells were harvested the next morning and resuspended into the 50 ml lysis buffer (20 mM HEPES, pH 7.4, 500 mM NaCl, 20 mM imidazole) with 1 mM phenylmethylsulfonyl fluoride and one tablet of Pierce protease inhibitor (ThermoFisher). The cells were sonicated for 5 min (10 s on, 30 s off), and the resulting lysate was further clarified by centrifugation at 40,000 × *g*, 1 h at 4°C. The supernatant was filtered by 0.22 μm Minisart Syringe Filter before loading into a 5 ml HisTrap HF column (GE Healthcare Life sciences) connected to the FPLC system (GE ÄKTA FPLC). The protein was eluted over a gradient injection of 500 mM imidazole. The collected protein peak fractions were further purified by size-exclusion chromatography using a HiLoad 16/600 Superdex200 column (GE Healthcare) in 20 mM HEPES, pH 7.4, 500 mM NaCl. The protein elution peak fractions were examined by the SDS–PAGE and followed by GelCode Blue Stain (ThermoFisher Scientific). The collected target proteins were concentrated and aliquoted to 5–10 μl each tube and frozen in liquid N_2.

To prepare monomeric G-actin, the purification procedure is described as before (Xie *et al.*, 2019). In brief, 2 g of rabbit muscle acetone powder was dissolved in 60 ml of ice-cold G-buffer (5 mM Tris, pH 8.0, 0.2 mM ATP, 0.1 mM $CaCl_2$, 0.5 mM dithiothreitol [DTT]) for 30 min, and the solution was filtered by cheesecloth to collect the actin-rich extracts. Such a procedure was repeated two more times on the dissolved rabbit muscle powder to collect a total of 180 ml actin-rich extracts. Furthermore, the actin-rich extract was subjected to centrifugation at 18,000 × *g*, and the supernatant was collected. To induce actin polymerization, 50 mM KCl and 2 mM $MgCl_2$ were added to the solution for 1 h. Subsequently, 0.8 M of KCl was added and stirred slowly for 30 min to remove actin-binding proteins. To collect polymerized actin filaments, the solution was subjected to centrifugation at 4°C, 95,800 × *g* for 3 h. Afterward, the F-actin pellets were transferred to the 10 ml homogenizer with a 7 ml G-buffer to be homogenized with the grinder. Furthermore, the F-actin was depolymerized by sonication with 3 s on and 10 s off, and such cycle was repeated four times, followed by dialysis against G-buffer for 1–2 d. We then performed centrifugation at 167,000 × *g* for 2.5 h to collect the top 2/3 supernatant and further purified through column HiPrep 16/60 SephacrylTM S-300 HR. The collected monomeric actin was then stored at 4 °C with 1 mM sodium azide added and used within 1 mo.

Actin assembly assay

The assembly reaction contains 2 μM G-actin with 5% pyrene actin (Cytoskeleton) where 3 μM yeast profilin was added. First, 10 μM G-actin was converted to Mg^{2+}-ATP-actin for 5 min on ice. Once the desired proteins were mixed with G-actin, the actin polymerization was initiated by adding 10× KME buffer mix (10 mM $MgCl_2$, 10 mM EGTA, and 500 mM KCl), at a total reaction volume of 120 μl. The pyrene-actin fluorescence signal was monitored in a plate reader Cytation 5 (BioTek, USA) at excitation and emission wavelengths of 365 and 407 nm, respectively. To determine the percentage increase in promoting formin activity (P), we first fitted line at the half polymerization of each reaction to reflect the actin assembly rate of each condition, and we calculated P based on function $(S_a\text{-}S_f)/S_f$, where S_a is the slope value of each NPF+formin condition and S_f is the slope value of formin. Afterward, hyperbola fitting function $P = B_{max}*c/(K_{app} + c)$ was used to determine the K_{app}, where c is the concentration of NPF, and $K_{app} = 0.5 * B_{max,}$ which corresponds to the concentration of NPF that is required for half-maximal stimulation of formin-mediated actin assembly. The values shown in the graph were the average data from three times of independent biological replicates experiments.

Fluorescence anisotropy

The fluorescence anisotropy assay was performed as previously described (Xie *et al.*, 2019). In brief, 60 nM Aip5C-Alexa Fluor 488 was mixed with Bnr1FH1C or Bnr1-C in an equal volume. The reaction buffer was 20 mM HEPES, pH 7.4, 150 mM NaCl, and proteins were incubated in low-volume nonbinding black 384-well plates at room temperature for 1 h. The plate reader Cytation 5 (BioTek, USA) with fluorescence polarization mode (excitation filter: 485 nm, 20 nm bandpass; emission filter: 510 nm, 20 nm bandpass) was used to record the parallel reading $I_{\parallel}$ and perpendicular reading $I_{\perp}$. The fluorescence anisotropy was then calculated by the following equation:

$$A = \frac{I\parallel - I\perp}{I\parallel + 2\,I\perp}$$

Furthermore, the fluorescence anisotropy value was normalized by blank reading and plotted against the corresponding ligand concentration in Prism Graphpad 8. The binding affinity K_D can be determined from the binding curves fitted with the Hill equation. The final graph was shown with means from three independent experiments.

TIRF microscopy

The TIRF microscopy experiment was performed as described before (Xie *et al.*, 2019). In brief, 25 × 50-mm coverslips (Marienfeld Superior) were soaked in 20% sulfuric acid overnight and rinsed thoroughly with sterile water. Afterward, the coverslips were coated with 2 mg/ml methoxy-PEG-silane (Mw: 2000; Laysan Bio) and 2 μg/ml biotin-PEG-silane (Mw: 3400; Laysan Bio) in 80% ethanol (pH 2.0, adjusted by HCl) at 70 °C for overnight. The next day, coverslips were rinsed thoroughly with sterile water and dried in N_2 stream, which can be kept at −80 °C for long-term storage. Before each experiment, the functionalized coverslip was attached to a plastic flow cell chamber (Ibidi, sticky-Slide VI 0.4). The flow cell was first incubated for 30 s with buffer HBSA (20 mM HEPES, pH 7.5, 1 mM EDTA, 50 mM KCl, and 1% bovine serum albumin), incubated for 60 s in 0.1 mg/ml streptavidin in buffer $HEKG_{10}$ (20 mM HEPES, pH 7.5, 1 mM EDTA, 50 mM KCl, 10% [vol/vol] glycerol). Finally, the flow cell chamber was washed with 1× TIRF buffer (10 mM imidazole, 50 mM KCl, 1 mM $MgCl_2$, 1 mM EGTA, 0.3 mM ATP, 50 mM DTT, 15 mM glucose, 100 μg/ml glucose oxidase, and 0.5% methylcellulose [4000 cP], pH 7.4). Proteins were mixed in TIRF buffer with 1 μM G-actin (10% Oregon Green 488 labeled, 0.5% biotin labeled) with 3 μM yeast profilin and then mixed with an equal volume of 2× TIRF buffer before flowing into the chamber. The still images were acquired at 4–5 min for quantifying actin nucleation seeds number; 5-s interval movies were acquired for 10 min using Apochromat TIRF 100× NA 1.49 (Nikon Instruments) on Nikon ECLIPSE Ti-S inverted microscope with iLAS2 motorized TIRF illuminator (Roper Scientific, Evry Cedex, France). The illumination source, microscope stage, and a Prime 95B sCMOS camera (Photometrics) were all under the control of MetaMorph 7.8 software (Molecular Device, Sunnyvale, CA). The focus was maintained using the Perfect Focus System. To measure actin filament elongation rate, the individual filament in each sample was traced manually for at least 2 min each. To quantify the formin-mediated elongation speed, we selected the fast-growing barbed end population, as profilin-actin has been well characterized to accelerate the formin-mediated elongation speed. The measured actin filament length was then divided by the corresponding time to determine the elongation rate. We used the conversion factor of 370 subunits per micrometer of F-actin to estimate the barbed end elongation rate.

All-atom MD simulation

The MD simulations were performed using the GROMACS 5.1.2 software (Van Der Spoel *et al.*, 2005). The protein structure information was derived from our previous structural studies and approaches (Tanaka *et al.*, 2008; Chen *et al.*, 2012; Deng *et al.*, 2012; Xie *et al.*, 2019, 2020). The Charmm36m force field (Huang *et al.*, 2017) was used to describe proteins with the TIP3P water model (Mackerell Jr *et al.*, 2004) for solvent molecules. The temperature of water and proteins was kept constant, coupled independently for each group of molecules at 300 K with a V-rescale thermostat (Bussi *et al.*, 2007). The pressure was coupled with a Parrinello-Rahman (Parrinello and Rahman, 1981) barostat at 1 atm separately in each of the three dimensions. The temperature and pressure time constants of the coupling were 0.1 and 2 ps, respectively. Integration of the equations of motion was performed by using a leapfrog algorithm with a time step of 2 fs. Periodic boundary conditions were implemented in all systems. A cutoff of 1 nm was implemented for the Lennard–Jones interactions and for the direct space part of the Ewald sum for Coulombic interactions. The Fourier space part of the Ewald splitting was computed by using the particle-mesh-Ewald method (Darden *et al.*, 1993) with a grid length of 0.16 nm and a cubic spline interpolation.

CD

Three hundred microliters of 0.15 mg/ml purified Bnr1-C and 0.075 mg/ml purified Bnr1-LC proteins were prepared in a buffer (50 mM phosphate-buffered saline, pH 7.4) and then loaded in the water-jacketed, 1-mm path length cylindrical quartz cuvette (Hellma). The CD spectra were collected using a Jasco J-710 spectropolarimeter at 1 nm resolution and a scan rate of 200 nm /min at room temperature. Reported molar ellipticities were calculated by subtracting the background spectrum in the Chriascan CD Spectrometer. The CD spectrum was then subjected to DichroWeb (http://dichroweb.cryst.bbk.ac.uk/html/home.shtml) with K2D program for secondary structure analysis (Whitmore and Wallace, 2004, 2008).

Yeast cell growth assay

The overnight culture of yeast cells was reinoculated into fresh YPD (10 g/l yeast extract, 20 g/l peptone, 20 g/l glucose) medium starting from O.D. 600 = 0.2 and allowed to grow to O.D. 600 around 0.8 to 1. Subsequently, 130 μl of cultures were added into a transparent 96-well plate with or without 1 μM LatA. Each condition was replicated four times and monitored at O.D. 600 every 15 min at 25°C. A constant shaking was maintained between each measurement to prevent cell precipitation. The O.D.600 was recorded by the plate reader Cytation 5 (BioTek, USA) for 20 h. To quantify the area size below each growth curve, O.D. 600 = 0.1 was used as the baseline; the area size was calculated by Prism Graphpad 8.

Live-cell fluorescence imaging

All yeast strains used in this study are listed in Supplemental Table S1. Yeast strains were cultured overnight at 25°C in the synthetic complete media + 2% glucose without tryptophan (to minimize auto-fluorescence) and reinoculated into fresh medium to culture until O.D. 600 = 0.6–0.8. Cells were then immobilized onto Concanavalin A (1 mg/ml)-coated coverslips and imaged by wide-field microscope Leica DMi8 (Leica Microsystems) equipped with an ORCA-Flash4.0 LT scientific CMOS camera (Hamamatsu Photonics, Japan) and a Leica× 100 oil immersion objective lens (NA 1.4). For whole-cell imaging, images were acquired continuously at a 0.25-μm interval for a total range of 7.5 μm in the z direction using an exposure time of 200 ms and 1× binning. To characterize actin cable phenotype, the maximum Z-projection images were created from live-cell imaging data by ImageJ.

In vivo concentration measurements for polarisome proteins

We have quantified in vivo protein concentration of Bud6 and Bnr1 using three reference strains expressing Syp1-GFP, Crn1-GFP, and Sec3-GFP as reference. The cytosolic protein concentrations of Syp1, Crn1, and Sec3 were previously determined by fluorescence cross-correlation spectroscopy (Boeke *et al.*, 2014; Picco *et al.*, 2017). Sum slices-Z projection images were used for intensity analysis. As previously reported, we measured the total cytosol signal intensity of reference and polarisome proteins from the ROIs of 10 × 10 pixels from 20 cells (Rowlinson and Widom, 2013). The same methods were used to measure the background and auto-fluorescence signal from the cytosol. A signal intensity standard curve and equation were derived from the reference cytosolic concentration and examined cytosolic signal of Syp1, Crn1, and Sec3. The cytosol concentrations of Bud6 and Bnr1 were calculated based on the above equation in Supplemental Figure S5, whereas tip concentration was derived from the signal intensity ratio.

Protein sequence analysis

Sequence alignment of formins (Bni1 and Bnr1) was carried out through the online server Clustal Omega (https://www.ebi.ac.uk/Tools/msa/clustalo/), and the figure was generated by software Jalview.

Statistical analysis

All statistical analyses were performed in GraphPad Prism 8. *P* values were determined by one-way analysis of variance (*$p < 0.05$, **$p < 0.01$, ***$p < 0.001$, ****$p < 0.0001$ and ns = no significant). Error bars indicate the SD.

Data availability

All data are contained within the manuscript.

ACKNOWLEDGMENTS

We thank Jessica Henty-Ridilla (SUNY Upstate Medical University) for sharing the actin preparation protocol. We thank the National Supercomputing Center Singapore (https://www.nscc.sg/) for assisting the computational work. This study was supported by a NTU startup grant (M4081533), Skin Research Institute of Singapore (SRIS, SIG18002), and MOE Tier 2 (MOE2016-T2-1-005), MOE Tier 3 (MOE2019-T3-1-012) to Y.M., and MOE Tier 1 (2018-T1-001-096) to L.L. in Singapore.

REFERENCES

Alford RF, Leaver-Fay A, Jeliazkov JR, O'Meara MJ, DiMaio FP, Park H, Shapovalov MV, Renfrew PD, Mulligan VK, Kappel K (2017). The Rosetta all-atom energy function for macromolecular modeling and design. J Chem Theory Comput 13, 3031–3048.

Bieling P, Mullins D, Fletcher D (2019). Force Regulation of Capping and Arp2/3 Nucleation of Branched Actin Networks. Biophys J 116, 252a.

Boeke D, Trautmann S, Meurer M, Wachsmuth M, Godlee C, Knop M, Kaksonen M (2014). Quantification of cytosolic interactions identifies Ede1 oligomers as key organizers of endocytosis. Mol Syst Biol 10, 756.

Breitsprecher D, Jaiswal R, Bombardier JP, Gould CJ, Gelles J, Goode BL (2012). Rocket launcher mechanism of collaborative actin assembly defined by single-molecule imaging. Science 336, 1164–1168.

Brühmann S, Ushakov DS, Winterhoff M, Dickinson RB, Curth U, Faix J (2017). Distinct VASP tetramers synergize in the processive elongation of individual actin filaments from clustered arrays. Proc Natl Acad Sci USA 114, E5815–E5824.

Bussi G, Donadio D, Parrinello M (2007). Canonical sampling through velocity rescaling. J Chem Phys 126, 014101.

Buttery SM, Yoshida S, Pellman D (2007). Yeast formins Bni1 and Bnr1 utilize different modes of cortical interaction during the assembly of actin cables. Mol Biol Cell 18, 1826–1838.

Campellone KG, Cheng H-C, Robbins D, Siripala AD, McGhie EJ, Hayward RD, Welch MD, Rosen MK, Koronakis V, Leong JM (2008). Repetitive N-WASP—binding elements of the enterohemorrhagic Escherichia coli effector EspF U synergistically activate actin assembly. PLoS Pathog 4, e1000191.

Case LB, Zhang X, Ditlev JA, Rosen MK (2019). Stoichiometry controls activity of phase-separated clusters of actin signaling proteins. Science 363, 1093–1097.

Chen H, Kuo CC, Kang H, Howell AS, Zyla TR, Jin M, Lew DJ (2012). Cdc42p regulation of the yeast formin Bni1p mediated by the effector Gic2p. Mol Biol Cell 23, 3814–3826.

Cheng KW, Mullins RD (2020). Initiation and disassembly of filopodia tip complexes containing VASP and lamellipodin. Mol Biol Cell 31, 2021–2034.

Chesarone MA, Goode BL (2009). Actin nucleation and elongation factors: mechanisms and interplay. Curr Opin Cell Biol 21, 28–37.

Clemens L, Dushek O, Allard J (2021). Intrinsic disorder in the T cell receptor creates cooperativity and controls ZAP70 binding. Biophys J 120, 379–392.

Darden T, York D, Pedersen L (1993). Particle mesh Ewald: An N· log (N) method for Ewald sums in large systems. J Chem Physics 98, 10089–10092.

Deng Y, Schmid N, Wang C, Wang J, Pessi G, Wu D, Lee J, Aguilar C, Ahrens CH, Chang C, *et al*. (2012). Cis-2-dodecenoic acid receptor RpfR links quorum-sensing signal perception with regulation of virulence through cyclic dimeric guanosine monophosphate turnover. Proc Natl Acad Sci USA 109, 15479–15484.

Disanza A, Bisi S, Winterhoff M, Milanesi F, Ushakov DS, Kast D, Marighetti P, Romet-Lemonne G, Müller HM, Nickel W (2013). CDC42 switches IRSp53 from inhibition of actin growth to elongation by clustering of VASP. EMBO J 32, 2735–2750.

Firat-Karalar EN, Welch MD (2011). New mechanisms and functions of actin nucleation. Curr Opin Cell Biol 23, 4–13.

Garabedian MV, Stanishneva-Konovalova T, Lou C, Rands TJ, Pollard LW, Sokolova OS, Goode BL (2018). Integrated control of formin-mediated actin assembly by a stationary inhibitor and a mobile activator. J Cell Biol 217, 3512–3530.

Glomb O, Bareis L, Johnsson N. (2019). YFR016c/Aip5 is part of an actin nucleation complex in yeast. Biol Open 8, bio044024.

Graziano BR, DuPage AG, Michelot A, Breitsprecher D, Moseley JB, Sagot I, Blanchoin L, Goode BL (2011). Mechanism and cellular function of Bud6 as an actin nucleation–promoting factor. Mol Biol Cell 22, 4016–4028.

Graziano BR, Jonasson EM, Pullen JG, Gould CJ, Goode BL (2013). Ligand-induced activation of a formin—NPF pair leads to collaborative actin nucleation. J Cell Biol 201, 595–611.

Harker AJ, Katkar HH, Bidone TC, Aydin F, Voth GA, Applewhite DA, Kovar DR (2019). Ena/VASP processive elongation is modulated by avidity on actin filaments bundled by the filopodia cross-linker fascin. Mol Biol Cell 30, 851–862.

Higgs HN, Pollard TD (2000). Activation by Cdc42 and PIP2 of Wiskott-Aldrich syndrome protein (WASp) stimulates actin nucleation by Arp2/3 complex. J Cell Biol 150, 1311–1320.

Huang J, Rauscher S, Nawrocki G, Ran T, Feig M, de Groot BL, Grubmüller H, MacKerell AD (2017). CHARMM36m: an improved force field for folded and intrinsically disordered proteins. Nat Methods 14, 71–73.

Li DW, Xie M, Bruschweiler R (2020). Quantitative Cooperative Binding Model for Intrinsically Disordered Proteins Interacting with Nanomaterials. J Am Chem Soc 142, 10730–10738.

Ma Z, Liu X, Nath S, Sun H, Tran TM, Yang L, Mayor S, Miao Y (2021a). Formin nanoclustering-mediated actin assembly during plant flagellin and DSF signaling. Cell Rep 34, 108884.

Ma Z, Miao Y (2020). Review: F-Actin remodelling during plant signal transduction via biomolecular assembly. Plant Sci 301, 110663.

Ma Z, Sun Y, Zhu X, Yang L, Chen X, Miao Y (2021b). Membrane nanodomains modulate formin condensation for actin remodeling in Arabidopsis innate immune responses. Plant Cell, koab261.

Machesky LM, Mullins RD, Higgs HN, Kaiser DA, Blanchoin L, May RC, Hall ME, Pollard TD (1999). Scar, a WASp-related protein, activates nucleation of actin filaments by the Arp2/3 complex. Proc Natl Acad Sci USA 96, 3739–3744.

Mackerell Jr AD, Feig M, Brooks III CL (2004). Extending the treatment of backbone energetics in protein force fields: limitations of gas-phase quantum mechanics in reproducing protein conformational distributions in molecular dynamics simulations. J Comput Chem 25, 1400–1415.

Miao Y, Han X, Zheng L, Xie Y, Mu Y, Yates III JR, Drubin DG (2016). Fimbrin phosphorylation by metaphase Cdk1 regulates actin cable dynamics in budding yeast. Nat Commun 7, 11265.

Miao Y, Tipakornsaowapak T, Zheng L, Mu Y, Lewellyn E (2018). Phosphoregulation of intrinsically disordered proteins for actin assembly and endocytosis. FEBS J 285, 2762–2784.

Miao Y, Wong CC, Mennella V, Michelot A, Agard DA, Holt LJ, Yates JR, Drubin DG (2013). Cell-cycle regulation of formin-mediated actin cable assembly. Proc Natl Acad Sci USA 110, E4446–E4455.

Moseley JB, Goode BL (2005). Differential activities and regulation of Saccharomyces cerevisiae formin proteins Bni1 and Bnr1 by Bud6. J Biol Chem 280, 28023–28033.

Moseley JB, Sagot I, Manning AL, Xu Y, Eck MJ, Pellman D, Goode BL (2004). A conserved mechanism for Bni1- and mDia1-induced actin assembly and dual regulation of Bni1 by Bud6 and profilin. Mol Biol Cell 15, 896–907.

Okada K, Bartolini F, Deaconescu AM, Moseley JB, Dogic Z, Grigorieff N, Gundersen GG, Goode BL (2010). Adenomatous polyposis coli protein nucleates actin assembly and synergizes with the formin mDia1. J Cell Biol 189, 1087–1096.

Ozaki-Kuroda K, Yamamoto Y, Nohara H, Kinoshita M, Fujiwara T, Irie K, Takai Y (2001). Dynamic localization and function of Bni1p at the sites of directed growth in Saccharomyces cerevisiae. Mol Cell Biol 21, 827–839.

Padrick SB, Cheng H-C, Ismail AM, Panchal SC, Doolittle LK, Kim S, Skehan BM, Umetani J, Brautigam CA, Leong JM (2008). Hierarchical regulation of WASP/WAVE proteins. Mol Cell 32, 426–438.
Parrinello M, Rahman A (1981). Polymorphic transitions in single crystals: A new molecular dynamics method. J Appl Phys 52, 7182–7190.
Pfender S, Kuznetsov V, Pleiser S, Kerkhoff E, Schuh M (2011). Spire-type actin nucleators cooperate with Formin-2 to drive asymmetric oocyte division. Curr Biol 21, 955–960.
Picco A, Irastorza-Azcarate I, Specht T, Boke D, Pazos I, Rivier-Cordey AS, Devos DP, Kaksonen M, Gallego O (2017). The In Vivo Architecture of the Exocyst Provides Structural Basis for Exocytosis. Cell 168, 400–412.e418.
Pollard TD (2007). Regulation of actin filament assembly by Arp2/3 complex and formins. Annu Rev Biophys Biomol Struct 36, 451–477.
Qiao Z, Sun H, Ng JTY, Ma Q, Koh SH, Mu Y, Miao Y, Gao YG (2019). Structural and computational examination of the Arabidopsis profilin-Poly-P complex reveals mechanistic details in profilin-regulated actin assembly. J Biol Chem 294, 18650–18661.
Quinlan ME, Hilgert S, Bedrossian A, Mullins RD, Kerkhoff E (2007). Regulatory interactions between two actin nucleators, Spire and Cappuccino. J Cell Biol 179, 117–128.
Rowlinson JS, Widom B (2013). Molecular Theory of Capillarity, Mineola, NY: Dover Publications.
Sallee NA, Rivera GM, Dueber JE, Vasilescu D, Mullins RD, Mayer BJ, Lim WA (2008). The pathogen protein EspF u hijacks actin polymerization using mimicry and multivalency. Nature 454, 1005–1008.
Segal M, Bloom K, Reed SI (2000). Bud6 directs sequential microtubule interactions with the bud tip and bud neck during spindle morphogenesis in Saccharomyces cerevisiae. Mol Biol Cell 11, 3689–3702.
Su X, Ditlev JA, Hui E, Xing W, Banjade S, Okrut J, King DS, Taunton J, Rosen MK, Vale RD (2016). Phase separation of signaling molecules promotes T cell receptor signal transduction. Science 352, 595–599.
Sun H, Qiao Z, Chua KP, Tursic A, Liu X, Gao YG, Mu Y, Hou X, Miao Y (2018). Profilin negatively regulates formin-mediated actin assembly to modulate PAMP-triggered plant immunity. Curr Biol 28, 1882–1895.e1887.
Sun H, Zhu X, Li C, Ma Z, Han X, Luo Y, Yang L, Yu J, Miao Y (2021). Xanthomonas effector XopR hijacks host actin cytoskeleton via complex coacervation. Nat Commun 12, 4064.
Tanaka Y, Sakamoto S, Kuroda M, Goda S, Gao YG, Tsumoto K, Hiragi Y, Yao M, Watanabe N, Ohta T, Tanaka I (2008). A helical string of alternately connected three-helix bundles for the cell wall-associated adhesion protein Ebh from Staphylococcus aureus. Structure 16, 488–496.
Tu D, Graziano BR, Park E, Zheng W, Li Y, Goode BL, Eck MJ (2012). Structure of the formin-interaction domain of the actin nucleation-promoting factor Bud6. Proc Natl Acad Sci USA 109, E3424–E3433.
Van Der Spoel D, Lindahl E, Hess B, Groenhof G, Mark AE, Berendsen HJ (2005). GROMACS: fast, flexible, and free. J Comput Chem 26, 1701–1718.
Vizcarra CL, Kreutz B, Rodal AA, Toms AV, Lu J, Zheng W, Quinlan ME, Eck MJ (2011). Structure and function of the interacting domains of Spire and Fmn-family formins. Proc Natl Acad Sci USA 108, 11884–11889.
Whitmore L, Wallace B (2004). DICHROWEB, an online server for protein secondary structure analyses from circular dichroism spectroscopic data. Nucleic Acids Res 32, W668–W673.
Whitmore L, Wallace BA (2008). Protein secondary structure analyses from circular dichroism spectroscopy: methods and reference databases. Biopolymers 89, 392–400.
Xie Y, Loh ZY, Xue J, Zhou F, Sun J, Qiao Z, Jin S, Deng Y, Li H, Wang Y, *et al*. (2020). Orchestrated actin nucleation by the Candida albicans polarisome complex enables filamentous growth. J Biol Chem 295, 14840–14854.
Xie Y, Miao Y (2021). Polarisome assembly mediates actin remodeling during polarized yeast and fungal growth. J Cell Sci 134, jcs247916.
Xie Y, Sun J, Han X, Turšić-Wunder A, Toh JD, Hong W, Gao Y-G, Miao Y (2019). Polarisome scaffolder Spa2-mediated macromolecular condensation of Aip5 for actin polymerization. Nat Commun 10, 1–18.
Xu Y, Moseley JB, Sagot I, Poy F, Pellman D, Goode BL, Eck MJ (2004). Crystal structures of a Formin Homology-2 domain reveal a tethered dimer architecture. Cell 116, 711–723.
Yarar D, Waterman-Storer CM, Schmid SL (2007). SNX9 couples actin assembly to phosphoinositide signals and is required for membrane remodeling during endocytosis. Dev Cell 13, 43–56.
Zheng P, Nguyen TA, Wong JY, Lee M, Nguyen T-A, Fan J-S, Yang D, Jedd G (2020). Spitzenkörper assembly mechanisms reveal conserved features of fungal and metazoan polarity scaffolds. Nat Commun 11, 1–13.
Zoncu R, Efeyan A, Sabatini DM (2011). mTOR: from growth signal integration to cancer, diabetes and ageing. Nat Rev Mol Cell Biol 12, 21–35.